RSC Applied Polymers

ROYAL SOCIETY OF CHEMISTRY

PAPER

View Article Online
View Journal

Cite this: DOI: 10.1039/d6lp00059b

Sustainable barrier coatings for food packaging with a built-in, redox-activated trigger for surface hydrophilization

Xiong Xiong, [a] Sulari Anthony,[b] Juliane Eberhardt,[c] Sabine Rosenfeldt,[d] Daniel Friedrich, [a] Stefan Peiffer, [e] Johannes C. Brendel, *[c] Tillmann Lueders *[b] and Josef Breu *[a]

Plastic pollution, particularly from single-use food packaging, has become a significant environmental challenge that requires mitigation by improving environmental degradability. Along this line, a redox-programmable barrier coating is introduced that combines an effective barrier during use with a post-use redox-triggered hydrophilization mechanism. Fully delaminated vermiculite (VMT) nanosheets were intercalated with poly(*N*-acryloyl thiomorpholine) ($PNAT_{30}$) to form one-dimensional Bragg-stack nanocomposite barrier coatings on poly(lactic acid) (PLA) substrates, yielding highly ordered, 2 μm thick coatings that drastically suppressed oxygen and water vapour transmission to meet state-of-the-art levels for high-end food packaging at elevated relative humidity. Structural Fe(III)/Fe(II) in VMT was furthermore utilized as an intrinsic redox catalyst as determined by Mößbauer spectroscopy under anoxic/oxic cycling. Exposure to active biomass of the Fe(III)-reducing *Geobacter metallireducens* reduced structural Fe(III). Reactive oxygen species (ROS), inferred to form *via* Fenton-type reactions upon successive reoxygenation, are proposed to oxidize hydrophobic thioether side chains in $PNAT_{30}$ to more hydrophilic sulfoxides, as supported by FTIR, Raman, and solid-state NMR spectroscopy. This molecular transformation triggered a pronounced, stepwise decrease in water contact angle and surface restructuring, evidencing *in situ* formation of a more hydrophilic coating surface. This is expected to increase post-use environmental accessibility and may facilitate eco-corona development and microbial attachment on derived microplastics (MPs), although direct degradation experiments were not performed in the present study. The concept of coupling mineral-induced tortuous-path barrier enhancement with ROS-activated sulfur chemistry provides a generally novel strategy for designing packaging materials that combine excellent in-use protection with a built-in trigger for post-use hydrophilization in redox-fluctuating environments such as sewage plants, soils or composting stacks.

Received 18th February 2026,
Accepted 3rd May 2026

DOI: 10.1039/d6lp00059b

rsc.li/rscapplpolym

Introduction

Plastic pollution has become a systemic problem, with packaging dominating plastic use and waste generation (~42% of primary non-fibre plastics are used in packaging, which also represents the largest waste stream).[1] Globally, only about 9% of plastic waste generated up to 2015 was recycled, whereas most of the remainder was landfilled or incinerated, or accumulated in the environment by unintentional or thoughtless littering.[1] Mismanaged waste contributes millions of tons of plastics to soils and the oceans each year, highlighting substantial end-of-life losses for disposable items such as food packaging.[2] Fragmentation and weathering further convert discarded packaging into microplastics (MP)[3] that are now widespread in soils, waters, and living organisms.[4–7] MP clearly have become a vital challenge from scientific, economic, and regulatory perspectives.[8–10] In particular, single-use food packaging, which is most prone to littering, must be rendered degradable at the end-of-life.[11–13]

Food packaging must protect food mechanically during handling and it must mitigate the deterioration of taste or haptics (*e.g.* the crunchiness of chips). Food quality largely determines the best before dates that in turn affect the extent

[a]*Bavarian Polymer Institute and Department of Chemistry, University of Bayreuth, Universitätsstr. 30, 95440 Bayreuth, Germany. E-mail: Josef.breu@uni-bayreuth.de*
[b]*Ecological Microbiology, Bayreuth Center of Ecology and Environmental Research (BayCEER), University of Bayreuth, 95440 Bayreuth, Germany. E-mail: tillmann.lueders@uni-bayreuth.de*
[c]*Macromolecular Chemistry I and Bavarian Polymer Institute (BPI), University of Bayreuth, 95440 Bayreuth, Germany. E-mail: johannes.brendel@uni-bayreuth.de*
[d]*Physical Chemistry I, University of Bayreuth, Universitätsstr. 30, 95440 Bayreuth, Germany*
[e]*Bayreuth Center of Ecology and Environmental Research (BayCEER), Department of Hydrology, University of Bayreuth, Bayreuth 95440, Germany*

of food losses.[11] Biodegradable polyesters have poor barrier properties for both hydrophobic (*e.g.* O_2, N_2, CO_2) and hydrophilic (H_2O) permeants. Typically, at 25 °C and 65% RH, a 25 μm film of polylactic acid (PLA) shows oxygen (OTR) and water vapour (WVTR) transmission rates of 711 $cm^3\ m^{-2}\ day^{-1}\ atm^{-1}$ and approximately 110 $g\ m^{-2}\ day^{-1}$, respectively.[14,15] While the extent and rate of swelling with water vapour depend strongly on the ester type, biodegradable polyesters generally can swell with water to some extent. Water acts like a plasticizer and will increase segment mobility and thus transmission rates not only for H_2O but concomitantly for O_2. Consequently, during usage, it is advantageous to have a more hydrophobic polyester. Degradation of biodegradable polyesters is, however, substantially hampered by this hydrophobic nature of the surface (Fig. S1), which induces slow formation of the eco-corona that allows enzymatic attack and catabolic mineralization to carbon dioxide and water to become efficient.[16,17] The formation of an eco-corona can be fostered by the prior alteration of surfaces by slow photo/thermo-oxidation, creating polar groups.[18] Rather than relying on uncontrolled sluggish weathering, a more effective strategy is to introduce oxidation sensitive functionalities into the polymer that can be triggered by conditions changing when the packaging is released into the environment after usage.

Even hydrophobic biodegradable polymers fail to meet barrier specifications for high-end food packaging such as that for potato chips or coffee beans. Only when compounded with high aspect ratio nanosheets can barrier specifications be met by imposing tortuous diffusion pathways.[19,20] Here, we apply a natural layered silicate, fully delaminated vermiculite (VMT), as a novel barrier filler (Scheme 1). Upon the utter delamination of VMT into monolayers,[11] nanosheets may be obtained with aspect ratios of around 9000. As in turn the barrier improvement according to Cussler scales with the square of the aspect ratio, the potential for barrier improvement of VMT[11] is more than 2000 times that of a natural montmorillonite with a typical aspect ratio <200.[20–22] Aside from the thrilling barrier improvement potential, VMT additionally holds promise for post-use surface activation of polymers in the environment: when Fe-bearing 2 : 1 layered silicates like VMT are exposed to anoxic environments, for instance during composting of food wastes or in sewage plants, structural Fe(III) will be used as an electron acceptor by anaerobic bacteria.[23] After being re-exposed to oxygen in a subsequent oxic cycle, ROS such as superoxide radicals ($^{\bullet}O_2$) and hydroxyl radicals ($^{\bullet}OH$) will be produced.[24,25] As ROS can even cause oxidative cleavage of carbon–carbon bonds in polymers,[26] VMT may not only improve the barrier properties of (bio-)degradable polymers to a level that meets the benchmarks for sustainable food packaging but also contribute to post-use surface alteration (chemical aging) of MPs, rendering them more hydrophilic and thus potentially more accessible for microbial degradation.[27] In this line, we apply VMT as a catalyst intrinsic to the surface coating that promotes chemical oxidation by ROS generated upon environmental anoxic/oxic cycles.[28] When structural iron in layered silicates is exposed to such redox cycles, the Fe(II) produced in the anoxic state upon exposure to O_2 in the oxic state will trigger Fenton-type oxidations even at ambient temperatures.[29] Such redox activity has been used in soil remediation and heterogeneous catalysis.[30]

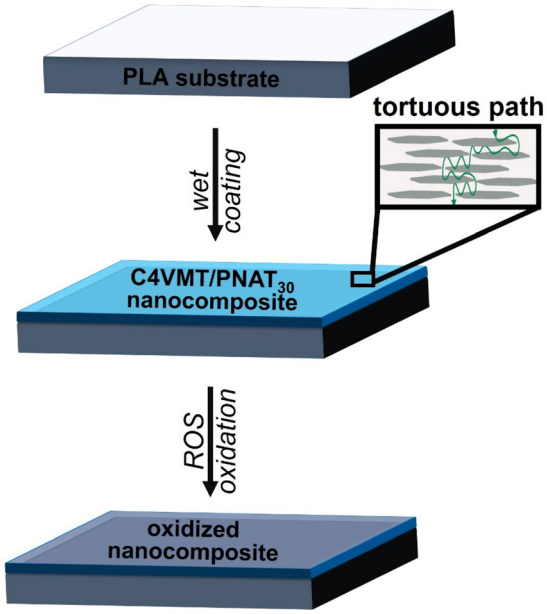

Scheme 1 The C4VMT/$PNAT_{30}$ coating on PLA: ensures an effective barrier during usage based on establishing a tortuous diffusion path, while in redox-cycling environments, oxidative surface hydrophilization by reactive oxygen species produced by structural iron is triggered.

In recent years, redox-responsive polymers have emerged as promising candidates for directing the end-of-life fate of functional materials.[28,31–33] Among other reactive groups, these materials exploit reactive sulfur motifs that undergo oxidation converting hydrophobic thioethers (–S–) into hydrophilic sulfoxides (–S(O)–) or sulfones ($–SO_2–$),[28] rendering the polymers more hydrophilic and more prone to swelling with water. In this line, poly(*N*-acryloyl thiomorpholine) (PNAT) was shown to undergo a hydrophobic-to-hydrophilic conversion upon oxidation by H_2O_2 allowing for dissolution of the initially hydrophobic polymer in water.[34]

Thus, in this work, we combine the two lines of thought detailed above: oxidative hydrophilization of a sulfur containing polymer triggered by ROS production from a compounded natural barrier filler after anaerobic microbial exposure. The contact angle of water with a barrier composite coating of $PNAT_{30}$ filled with VMT on PLA could be substantially lowered by both chemical and microbial reduction of structural iron that upon subsequent exposure to oxygen produced ROS capable of oxidizing (–S–) to (–S(O)–). The delaminated VMT nanosheets not only imposed long tortuous pathways that substantially suppressed O_2 and H_2O transport, but also, through concomitantly structural Fe(III)/Fe(II) redox chemistry, activated a built-in formation mechanism of a hydrophilic chemical corona by ROS catalysis.

Results and discussion

Bragg-stack composite *via* polymer intercalation and its barrier performance

When butylammonium-VMT (C4VMT) is immersed in *N*-methylformamide (NMF), it spontaneously and thermodynamically delaminates into monolayer nanosheets. Due to the large diameter of the nanosheets, their rotation is hampered even at concentrations as low as 2 wt% and a lamellar liquid crystalline (nematic) suspension is obtained instead of an isotropic suspension. Next, the nematic C4VMT suspension is mixed with a solution (2 wt% in dimethylformamide (DMF)) of $PNAT_{30}$ with a low degree of polymerization (30 repeating units) for effective intercalation and to minimize the confinement penalty. The nematic nature of the suspension is preserved upon addition of the polymer solution as indicated by birefringence (Fig. 1a inset). Successful delamination and the nematic nature of the suspension were, moreover, cross-checked by the small-angle X-ray scattering (SAXS, Fig. 1a). For intensity reasons, the suspension was concentrated by centrifugation to 5 wt%. The scattering of nanosheets is confirmed by a q^{-2} dependency of the intensity; a 00*l* series confirms a co-planar arrangement of nanosheets separated to 48 nm at this concentration, and the lack of a peak at high q values corresponding to C4VMT stacks proves utter delamination. The SAXS pattern was calculated using a model of 1D stacked discs (Fig. 1a green line) with a diameter of 9000 nm and a thickness of 1 nm. The diameter was taken as in line with the average diameter of nanosheets as determined by static light scattering (SLS, Fig. S2). The liquid crystalline nature of the coating suspension is a prerequisite for perfect texture and the 1D crystalline order of the nanocomposite coating. The liquid crystalline nature is defined by the concentration of the clay in the suspension and the aspect ratio. As the viscosity of the suspension quickly increases with vermiculite concentration, an appreciable aspect ratio is required to ensure the nematic nature of the suspension and to obtain the Bragg-stack structure and the superb barrier performance related to it.[19,20]

Nanocomposite coatings with approximately 2 μm dry thickness were applied by doctor-blading a 100 μm thick wet-coat at RT on a PLA film (25 μm).[35,36] Upon drying at 50 °C overnight, the X-ray diffraction (XRD) pattern of the dry coating reveals a 19 Å *d*-spacing (Fig. 1b). The observation of a rational 00*l* series indicates a one-dimensional (1D) crystalline monodomain of a hybrid Bragg-stack. Upon drying, individual VMT nanosheets (1 nm thick) are oriented coplanar to the substrate in a largely overlapping mode with the same amount of polymer volume (0.9 nm thick layers) intercalated between. This ordered polymer intercalation required a careful iterative adjustment of nanosheet to polymer volume with the latter amounting to 47 vol%. The polymer is of course severely confined between the nanosheets. Cross-sectional transmission electron micrographs (TEM, Fig. 1c) confirm a highly periodic hybrid Bragg-stack structure with uniform interlayer spacing (~2 nm), in excellent agreement with the XRD pattern obtained for the film. According to Cussler models, such textured nanocomposites of large aspect ratio nanosheets substantially elongate the gas diffusion pathway ('tortuous path') since permeating gas molecules must circumvent thousands of high-aspect-ratio impermeable nanosheets.[19,20]

The barrier performance of the uncoated PLA film (BoPLA P01001, supplied by Pütz Folien) for O_2 and water vapour is quite moderate,[15] especially at elevated relative humidity.[37,38] According to the company's data sheet, a 25 μm PLA foil shows an OTR of 900 cm^3 m^{-2} day^{-1} bar^{-1} (23 °C, 0% RH, ASTM D3985) and a WVTR of 330 g m^{-2} day^{-1} (38 °C, 90% RH, ASTM F1249), values that render neat PLA inappropriate for food packaging.[39] In the present study, PLA was used as a representative biodegradable polyester substrate to evaluate the barrier-enhancing effect of the $C4VMT/PNAT_{30}$ coating. Only the surface modification of the barrier coating was, however, investigated in this study rather than the degradation of the complete packaging including the substrate. The 2 μm

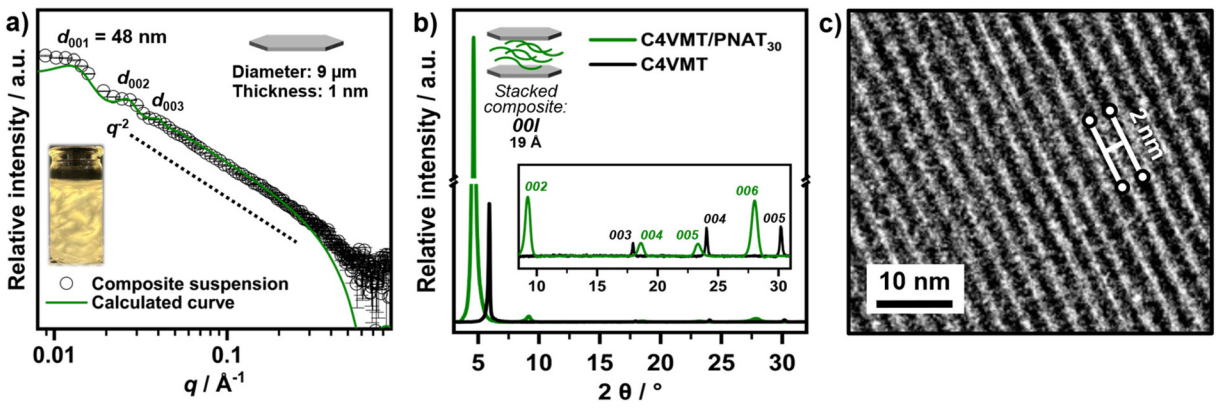

Fig. 1 (a) SAXS pattern of a 5 wt% $C4VMT/PNAT_{30}$ suspension in NMF. The dotted line shows a q^{-2} scaling. Inset: photograph of the birefringent suspension under cross-polarized light. (b) XRD pattern of a C4VMT film and a dry $C4VMT/PNAT_{30}$ nanocomposite coating. (c) TEM image of a cross section of a dry $C4VMT/PNAT_{30}$ nanocomposite coating.

thick C4VMT/$PNAT_{30}$ Bragg-stack nanocomposite coating substantially improved the barrier. Specifically, the coated PLA film showed an OTR of 1.70 cm^3 m^{-2} day^{-1} bar^{-1} and a WVTR of 1.68 g m^{-2} day^{-1} (both measured at 25 °C, 65% RH). These transmission rates are comparable to values observed for biodegradable nanocomposite coatings made from VMT/PLA nanocomposites and meet even cutting edge food packaging requirements.[11]

$PNAT_{30}$ oxidation by chemically reduced VMT nanosheets

The biodegradation of MP requires the formation of an eco-corona. For instance, PLA biodegradation primarily occurs through hydrolytic and enzymatic processes by fungi and bacteria, secreting enzymes like polyesterases, esterases, and cutinases that break ester bonds. Fungi such as *Pleurotus*, *Penicillium*, and *Aspergillus* spp. degrade PLA effectively, with mycelial penetration enhancing substrate access. Coronas (chemically modified surfaces) indirectly affect this by altering PLA surface polarity, potentially facilitating microbial attachment in the plastisphere.[40] As outlined in the introduction, formation of an eco-corona can be fostered by a prior alteration of surfaces by slow photo/thermo-oxidation creating polar groups.[18] Rather than relying on sluggish uncontrolled weathering, we introduce oxidation sensitive functionalities into the polymer while applying a VMT barrier filler as an intrinsic catalyst promoting chemical oxidation by ROS generated upon environmental anoxic/oxic cycles.[28]

As the amount of sample in a 2 μm thick coating is minute, we first strove for a proof of concept by blending a solution of $PNAT_{30}$ in DMF with a suspension of reduced C4VMT (R-C4VMT) in NMF. Next, oxidation was abiotically triggered by bubbling O_2 through the suspension (Fig. 2a). Upon contact with O_2, structural Fe(II) sites are expected to promote ROS-mediated heterogeneous Fenton-like[41–45] oxidation of thioether units in the $PNAT_{30}$ polymer. The C4VMT was then centrifuged and reduced again, exposing the $PNAT_{30}$ polymer to 4 more redox cycles.

The oxidized $PNAT_{30}$ was precipitated by adding acetone as an antisolvent to the DMF/NMF supernatant and finally dried in a vacuum oven at 40 °C overnight. Successful oxidation was checked by Fourier transform infrared spectroscopy (FTIR, Fig. 2b), where a prominent band at 1051 cm^{-1} indicates a sulfoxide function[46,47] produced by oxidation of the thioether group. The carbonyl band[51] at ~1633 cm^{-1} and the higher-frequency fingerprint region remained essentially unchanged, indicating that the backbone of the polymer remained unaffected. Raman spectroscopy (Fig. 2c) provides additional evidence for the oxidative thioether conversion. Upon redox cycling of $PNAT_{30}$, the C–S stretching bands at 630–750 cm^{-1} decreased in intensity, which reflects the gradual conversion of thioether groups. New and strong features appeared in the 1030–1170 cm^{-1} region, which is assigned to the Raman-active S═O vibrations of sulfoxides.[48,49] Solid-state ^{13}C CP/MAS NMR (Fig. 2d) also supported successful oxidation of the thioether group. The main resonance of the α-carbons next to the thioether located at 45–50 ppm showed a small but significant downfield shift and an increase in intensity in the oxidized sample. Such spectral changes are in line with previous

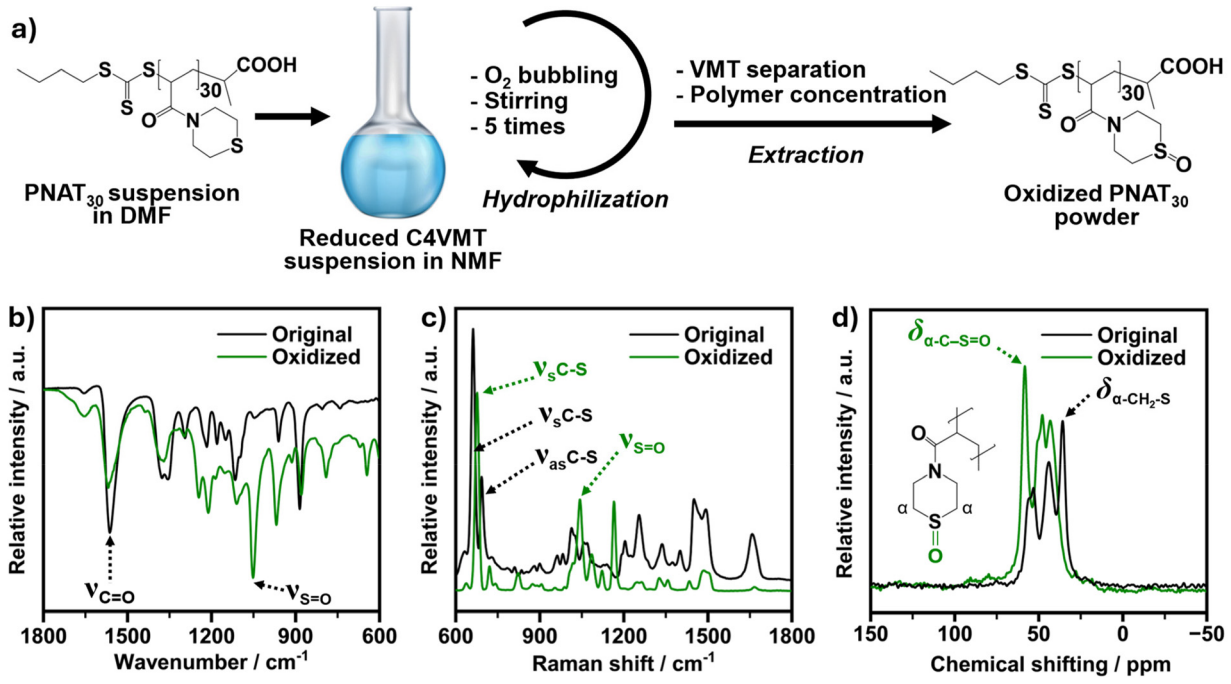

Fig. 2 (a) Proposed scheme of $PNAT_{30}$ oxidation by ROS inferred to arise during VMT redox cycling. (b) FTIR spectra of $PNAT_{30}$ before and after oxidation. (c) Raman spectra of $PNAT_{30}$ before and after oxidation. (d) ^{13}C CP MAS NMR spectra of $PNAT_{30}$ before and after oxidation. Inset: chemical structure of the oxidized $PNAT_{30}$ repeating unit, highlighting the α-carbon environments corresponding to the assigned resonances.

reports on selective thioether oxidation in polymers and small-molecule analogues.[50] This downfield shift indicates a more electron-withdrawing environment at α-carbons after oxidation, while the rest of the spectrum remains nearly unchanged. In summary, all these spectral features are consistent with selective oxidation of the thioether without changes to the polymer backbone of $PNAT_{30}$ mediated by anoxic/oxic cycling of C4VMT. The oxidation potential of ROS certainly is strong enough so that further oxidation to sulfone is expected. Experimentally, only oxidation to sulfoxide was observed, a fact that is attributed to substoichiometric production of ROS within the limited number of redox cycles applied. In the same line, most likely, the RAFT end group will also be oxidized, which, however, could not be identified experimentally.

Modification of surface hydrophilicity *via* redox cycling of C4VMT/$PNAT_{30}$ coatings

Next, changes in the wetting angle of C4VMT/$PNAT_{30}$ of barrier coatings were monitored with exposure to environmental anoxic/oxic redox cycling. In line with biotic environmental exposure, cycling was driven by anaerobic bacteria capable of reducing structural iron. After the Bragg-stack coating was prepared, it was completely immersed in a culture medium under strictly anaerobic conditions and inoculated with *Geobacter metallireducens* to trigger biological reduction of structural Fe (III).[51] After at least 24 h, the film was removed from the culture medium and exposed to the atmosphere for 2 h to activate the Fenton-type oxidation (Fig. 3a). ^{57}Fe Mößbauer spectra

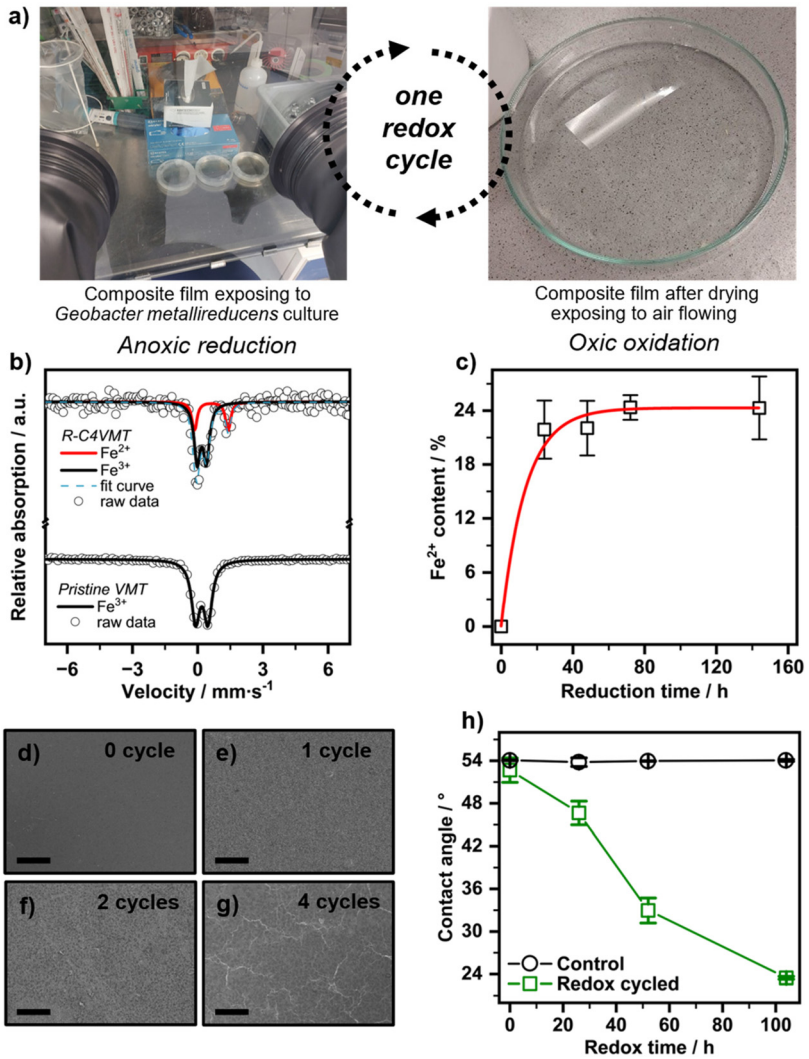

Fig. 3 (a) Redox cycling of the C4VMT/$PNAT_{30}$ Bragg-stack coating on a PLA substrate: the film is first immersed in a culture medium inoculated with *Geobacter metallireducens* under strictly anaerobic conditions to induce biotic reduction of structural Fe(III) of C4VMT nanosheets. Subsequently, the film is removed from the medium and exposed to the atmosphere. (b) Mößbauer spectra of the C4VMT nanosheets after being suspended in the culture medium with *Geobacter metallireducens*, showing the partial reduction of structural Fe(III) to Fe(II). (c) Monitoring of the Fe (II) fraction with time during which the coating was suspended in the bacterial medium. (d–g) Scanning electron microscopy (SEM) images of the surface of the (d) pristine barrier coating and after (e) 1, (f) 2, and (g) 4 redox cycles (scale bars: 100 μm). (h) Change of contact angle of the coating surface with water with the number of exposures to culture media with and without inoculation of *Geobacter metallireducens*.

(Fig. 3b and Table S1) recorded before and after exposure to air provided quantitative evidence of partial structural Fe(III) reduction by bacteria under anoxic conditions (Fig. 3b, R-C4VMT). While with pristine VMT all structural Fe was Fe(III) (Fig. 3b, Pristine VMT), biotic reduction produced an octahedral Fe(II) doublet (red line, chemical shift (CS): 1.51 mm s^{-1}, quadrupole splitting (QS): 2.88 mm s^{-1}), which is within the expected range for structural Fe(II) in layered silicates.[52–54] Time-resolved monitoring of the Fe(II) fraction (Fig. 3c and Table S2) showed a rapid increase approaching saturation after 24 h, when 24% of structural Fe(III) had been reduced.

SEM (Fig. 3d–g) images of the coating surface furthermore indicated increasing morphological changes of the polymer with successive redox cycles. Specifically, the pristine surface appeared compact and smooth, without detectable defects or cracks before redox cycling. Already after the first redox cycle, nanoscale roughening and shallow pits developed (Fig. 3e and f), indicating surface restructuring or morphological changes as redox alteration proceeded. After four cycles, interconnected cracks became evident throughout the entire surface (Fig. 3g). These microstructural changes observed in the coatings are consistent with the built-in chemical formation of a more hydrophilic surface. Oxidation of the thioether bonds into sulfoxides of $PNAT_{30}$ leads to a more hydrophilic surface that is expected to increase swelling with water and this in turn causes appreciable mechanical stress, causing the cracking (Fig. 3d–g). SEM images (Fig. S8) of the surface of samples exposed four times to the culture medium without inoculation of *Geobacter metallireducens* and hence without oxidative hydrophilization show no visible cracking. This indicates that the mechanical stress induced by the limited swelling of pristine $PNAT_{30}$ causes no crack formation. The increased hydrophilicity with redox cycling of the coating was moreover evidenced by the progressive and substantial decrease in the contact angle of the composite film surface (Fig. 3h) that had been oxidized after anoxic microbial reduction followed by air exposure. The pristine nanocomposite coating showed a large contact angle with water of 54° as expected for a hydrophobic $PNAT_{30}$ matrix (Fig. S4). The contact angle decreased with each redox cycle, becoming as low as 24° after 4 cycles (Fig. 3h and Fig. S5–S7), indicating a substantially more polar surface. This change may not be attributed to the exposure to culture media alone (Fig. 3h, control) as this does not show a change in contact angle. The inoculation of *Geobacter metallireducens* triggering the reduction of structural Fe(III) was essential for observing the change in contact angle. The polar surface of the coating is expected to increase post-use wettability, which may facilitate subsequent microbial attachment. The change in contact angle for the coating is, however, primarily driven by the built-in chemical formation of an abiotic corona rather than external factors such as passive adsorption or polymer relaxation.[55,56] While barrier performance was only measured for the pristine coating in the present study, the observed increase in hydrophilicity, surface roughening, and crack formation after redox cycling would be expected to impair the compact Bragg-stack architecture and thus deteriorate barrier performance.

Conclusion

The primary goal of this study was to modify the hydrophobic coating surface as required for barrier performance during usage into a hydrophilic surface that fosters eco-corona formation and ultimately biodegradation of the complete packaging including the PLA substrate. As quantitative oxidation is not relevant, fluxes and timescales are therefore unrelated.

The Bragg-stack nanocomposite coatings developed in this work demonstrate that fully delaminated natural VMT nanosheets can be used to convert intrinsically poor-barrier, biodegradable polyester substrates into high-performance food packaging films while simultaneously programming their surface for environmentally triggered hydrophilization. The C4VMT/$PNAT_{30}$ coatings form highly ordered one-dimensional Bragg-stacks with nanometre-scale polymer interlayers, yielding oxygen and water vapour transmission rates that match high-end food packaging benchmarks at elevated relative humidity despite a coating thickness of only about 2 μm. Through redox cycling of structural Fe(III)/Fe(II) in VMT, VMT-mediated ROS oxidize thioether units in $PNAT_{30}$ to sulfoxides, as inferred from complementary FTIR, Raman, and solid-state NMR analyses and supported by literature reports on Fe-bearing clay redox chemistry.[24,25,29,30] This molecular-level oxidation translates into macroscopic surface restructuring forming cracks and a pronounced decrease in water contact angle from initially hydrophobic values to around 24°, indicating the *in situ* formation of a more hydrophilic coating surface that may facilitate subsequent microbial attachment and eco-corona development on MPs derived from such coatings. The key innovation is the integration of barrier enhancement and redox-responsive sulfur chemistry within a single mineral–polymer architecture. This approach offers a materials design concept for packaging that protects food during use but, after release into fluctuating anoxic/oxic environments, becomes more wettable and microbially accessible, thereby helping to reconcile performance requirements with an accelerated and more controllable end-of-life fate. Questions regarding the environmental toxicity, persistence, and possible release of coating components, particularly after weathering or redox-activated structural alteration, were beyond the scope of the present study and will require dedicated investigation in future work. Moreover, direct degradation studies will be required to determine whether the observed surface hydrophilization of the coating translates into accelerated degradation of the coated polymer system under specific environmental conditions. In conclusion, our work provides a promising approach for developing high-performance and environmentally friendly food packaging materials.

Materials and methods

Materials

The VMT, obtained from a German importer, Isola, originated from a mine in Africa (IV-DB-DEU-Uganda-Namekara-2022-V2.

pdf). According to the composition given by the supplier, the structural formula of a half unit cell is $[Mg_{0.37}]^{inter}[Mg_{2.44}Fe_{0.46}]^{oct}[Si_{3.15}Al_{0.85}]^{tet}O_{10}(OH)_2$. The cation exchange capacity as measured photometrically *via* $[Co(en)]^{3+}$ exchange was found to be 186 meq/100 g. Natural VMT flakes were first ground and sieved to sizes <100 μm. All other chemicals used were supplied by Sigma-Aldrich: LiCl (≥99%), butylamine (≥99.5%), sodium citrate dihydrate (≥99%), L-ascorbic acid (≥99%), and citric acid (≥99%).

Cation exchange and delamination

The ground VMT was suspended in 100 mL of a 2 M (or 400 times the CEC) solution of butylamine (C4) titrated with citric acid to pH 7 and refluxed for 24 hours. The high ionic strength inhibits delamination. After five rounds of washing and centrifugation with a 50/50 vol% water/ethanol combination (again, the ethanol concentration inhibits spontaneous delamination), the VMT was dried in a vacuum oven at 70 °C. A rational 00*l* series with a very small coefficient of variation (CV) of 0.13% indicates complete C4 exchange.[57] Upon suspending C4-vermiculite (C4VMT) in NMF, it spontaneously delaminated into a nematic suspension. Delamination was completed within 24 hours in an overhead shaker at room temperature (RT) and a birefringent suspension was obtained.

Chemical reduction of structural iron in VMT

The C4VMT samples (0.5 g, equivalent to 0.56 mmol structural Fe) were delaminated by resuspending in 20 mL of deoxygenated, Ar-saturated water (concentration of the suspension 2 wt%). To this suspension, 20 mL of a 100 mM ascorbate solution was added, yielding a total volume of 40 mL with a 50 mM ascorbate concentration, equivalent to 2.0 mmol ascorbate in the suspension. Ascorbate was applied at a molar excess of approximately 3.6 times relative to structural Fe. After 12 h, 30% of the structural Fe(III) was reduced to Fe(II) as evidenced by Mößbauer spectroscopy (Fig. S3).

Reduction of structural iron in VMT by *Geobacter metallireducens*

Geobacter metallireducens[58] is a metal-reducing bacterium capable of growth *via* complete oxidation of organic substrates coupled to dissimilatory Fe(III) reduction. The strain used in this study (GS-15/ATCC 53774/DSM 7210) was obtained from the Leibniz Institute DSMZ – German Collection of Microorganisms and Cell Cultures in Braunschweig, Germany. *G. metallireducens* was cultivated for biomass generation under strictly anoxic conditions in Bellco 27 mL headspace vials sealed with 20 mm crimp stoppers using the DSMZ medium 579. The medium was prepared with (per L) 13.70 g of ferric citrate monohydrate, 1.50 g of NH_4Cl, 0.60 g of $NaH_2PO_4{\cdot}H_2O$, 0.10 g of KCl, and 2.50 g of sodium acetate. After autoclaving and cooling under an N_2/CO_2 (80 : 20, v/v) atmosphere, 2.50 g L^{-1} $NaHCO_3$ buffer was added under N_2/CO_2. Subsequently, the following components were added from sterile, anoxic stock solutions: 10 mL L^{-1} vitamin solution (DSMZ medium 141) and 1 mL L^{-1} modified Wollin's mineral solution (DSMZ medium 120). The pH of the final medium was adjusted to 6.7–7.0. The culture was grown to an OD_{600} of ~1.6 over 10 days at 30 °C in the dark.

Microbial VMT reduction incubations

Next to standard growth media described above, separate stocks of DSMZ medium 579 were prepared without ferric citrate as the electron acceptor. Here, structural Fe(III) of the VMT nanofiller incorporated into the C4VMT/$PNAT_{30}$ Bragg-stack coatings served as the sole electron acceptor. The coatings on PLA films (~3 cm^2) were placed into standard Petri dishes containing 20 mL of ferric citrate-omitted culture medium and inoculated with 1 ml of pre-grown cells of the active culture of *G. metallireducens*. Incubation was carried out within an anaerobic chamber (Mecaplex, Grenchen, CH) flushed with N_2 to allow for biotic reduction of iron in the nanosheets. For a single reduction cycle, nanosheets comprised within the coating were incubated for 24 h at room temperature in the anoxic chamber. Subsequently, the coated PLA films were removed from the culture medium and exposed to ambient air for 2 h to induce Fenton-type oxidative reactions. Reduction cycles 2 to 4 were performed by repeating the cycling two to four times, respectively, by re-exposing the coated PLA films to fresh biomass of *G. metallireducens* in fresh ferric citrate-omitted culture medium within the anaerobic chamber. After final re-oxidation, nanosheets were dried at 30 °C in the dark before downstream analysis.

Synthesis of poly(*N*-acryloylthiomorpholine) ($PNAT_{30}$)

$PNAT_{30}$ was prepared following established procedures.[59] Briefly, 2-(butylthiocarbonothioylthio)propanoic acid (PABTC, 2.12 mL of a 0.5 M solution in 1,4-dioxane, 1.06 mmol), *N*-acryloylthiomorpholine (5.0 g, 31.8 mmol), the radical initiator VA-044 (0.86 mL of a 20 mg mL^{-1} solution in Milli-Q water, 53.2 μmol) and 1,3,5-trioxane (20 mg) were combined in a 5 mL microwave vial and sealed with a rubber septum. After deoxygenation by argon bubbling for 20 min, the vial was placed in a preheated oil bath at 70 °C and stirred for 24 h, until monomer conversion was confirmed by ^1H NMR analysis (0.1 mL aliquot in $CDCl_3$). The reaction mixture was cooled to room temperature and precipitated in diethyl ether (300 mL). The product was dried under reduced pressure at 40 °C for 24 h. A number average molar mass (M_n) of 1.8 kg mol^{-1} and a dispersity ($Đ$) of 1.13 were determined by size exclusion chromatography (SEC) (eluent: DMAc + 0.21 wt% LiCl, calibration with PEO standards). The corresponding SEC trace and an ^1H-NMR spectrum of the polymer are given in the SI (Fig. S9).

Fabrication of the Bragg-stack nanocomposite barrier coating

The C4VMT/$PNAT_{30}$ suspension was applied on PLA films as a wet coat, which was prepared by mixing a 10 wt% $PNAT_{30}$ solution in DMF with a 5 wt% VMT dispersion in a mixture of γ-butyrolactone and NMF (γ -BL/NMF: 90 : 10) followed by mixing overnight on an overhead mixer.[11] The highly ordered 1D crystalline hybrid Bragg-stack requires a careful, iterative optimization of the clay-to-polymer ratio. The optimum was

found for a polymer weight fraction of around 30 wt% corresponding to 47 vol% taking the different densities for the polymer and clay into account. A wet coat (6.67 wt% solid content) of 100 μm was applied to a PLA substrate (25 μm supplied by Pütz Folien GmbH) by doctor blading (K Control Coater K202*, RK PrintCoat Instruments Ltd, United Kingdom). The substrate temperature was maintained at RT, while the blade speed was 3 cm s^{-1}. The coated foils were dried overnight at RT followed by drying at 40 °C in a vacuum oven for two days. The coating thickness of 2 μm was determined using a high-accuracy Digimatic micrometer (Mitutoyo, Japan) with a measuring range of 0–25 mm and a resolution of 0.0001 mm.

Mößbauer spectroscopy

The evolution of microbial reduction of VMT with time was followed by taking 20 mL of suspension at chosen time steps. The reduced VMT was washed with deionized, de-oxygenated and Ar-saturated water and centrifuged under an inert atmosphere in a glovebox. Approximately 0.20 g of powder was packed in the glovebox into a circular sample holder. Samples were sealed with Kapton film to mitigate re-oxidation and were immediately measured.

^{57}Fe Mößbauer spectra were recorded in transmission geometry at 295 ± 2 K within a sampling time of less than 12 h. Mößbauer spectra were collected with a configuration designed for high-resolution measurements. The setup consisted of a WissEl Mößbauer Drive System MR-360, an MA-260 velocity transducer for precise and controlled motion of the ^{57}Co(Rh) source (activity: ~50 mCi), and a KETEK silicon drift detector AXAS-M. The gain and shaping time constants were optimized experimentally. Data were collected using a CMCA-550 module in MCS [WINDOW] mode, enabling the selective detection of the 14.4 keV Mößbauer line. Calibration was carried out using a ^{57}Fe-enriched metallic foil. Measurements were taken at RT. The sinusoidal velocity waveform for the source motion was generated using a DFG-1000 digital function generator, which was synchronized with the CMCA-550 channel sweep. Spectral data were processed and analysed with MossA software to ensure accurate alignment and energy calibration.[60] Lorentzian line shapes were applied to fit the doublets. No constraint was applied.

X-ray diffraction

CuK_α radiation (λ = 1.54187 Å) was used to collect XRD data applying a Bragg–Brentano-type diffractometer (Empyrean, Malvern Panalytical BV, the Netherlands) fitted with a PIXcel-1D detector. The HighScore Plus program from Malvern Panalytical was used for peak search.

Small angle X-ray scattering

A "Double Ganesha AIR" (SAXSLAB/Xenocs) was used to record small angle X-ray scattering (SAXS) data. This laboratory-based system uses a rotating copper anode (MicroMax-007 HF, Rigaku Corporation, Japan) to produce a focused X-ray beam and a position-sensitive detector (PILATUS 300K, Dectris). The scattering vector range q = 0.0024–1.05 A^{-1} was covered. The C4VMT suspensions were added into 1 mm glass capillaries (Hilgenberg, code 4007610) for measuring. The data were circularly averaged and adjusted to account for the measurement duration, sample thickness, and incident beam. For background subtraction, a capillary filled with solvent was measured. Scatter (version 2.5) was used for further examination.

Static light scattering

A HORIBA LA-950 SLS device was applied to record the hydrodynamic radii distribution of aqueous dispersions by static light scattering (SLS). The solid phase's refractive index was assumed to be 1.5.

Transmission electron microscopy

Cross-sectional transmission electron microscopy (TEM) images were measured by employing a JEOL-JEM-2200FS (JEOL GmbH, Germany) microscope. Cross-sections of the nanocomposite coating were prepared by using a JEOL EM-09100IS Cryo Ion Slicer (JEOL GmbH, Germany).

Fourier-transform infrared spectroscopy

For Fourier-transform infrared spectroscopy (FTIR) measurements, a Jasco FTIR 6100 spectrometer was used.

Raman spectroscopy

Raman spectra were acquired in confocal geometry using a Horiba Jobin Yvon Raman spectrometer equipped with an Olympus BX41 microscope (50× magnification) and a He–Ne laser (11.5 mW laser power, λ = 633 nm). The spectra were recorded in the spectral range of 50–3500 cm^{-1} by summation of 20 individual spectra (5 s exposure time) using the LabSpec 5 software.

Solid-state NMR spectroscopy

The polymer samples before and after oxidation were measured with a spectrometer Bruker Avance III 400 (Magnetic Field 9.4 T). The solid state ^{13}C NMR MAS spectra were obtained using a ramped cross-polarization (CP) experiment, where the nutation frequency on the proton channel varied linearly by 50%. The samples were spun at 20.0 kHz in a 3.2 mm MAS triple resonance probe. The corresponding nutation frequency on the ^{13}C channel and the contact time were adjusted to 70 kHz and 1 ms, respectively. During acquisition, proton broadband decoupling was applied using a spinal-64 sequence with a nutation frequency of 60 kHz. The ^{13}C spectra are referenced indirectly with respect to tetramethylsilane (TMS) using adamantane as the secondary reference.

Oxygen transmission rate

The oxygen transmission rate (OTR) was determined on a Mocon OX-TRAN 2/21 M10× system (Mocon Inc., USA) with a lower detection limit of 5 × 10^{-4} cm^3 m^{-2} day^{-1} atm^{-1}. The measurements were performed at 23 °C and 65% RH. A mixture of 98 vol% nitrogen and 2 vol% hydrogen was used as the carrier gas and pure oxygen as the permeant (>99.95%, Linde Sauerstoff 3.5).

Water vapour transmission rate

The water vapour transmission rate (WVTR) was determined on a HiBarSens HBS 2.0 HT (Sempa Systems GmbH, Dresden, Germany) with a lower detection limit of 10^{-6} g m^{-2} day^{-1}. The tests were conducted at 23 °C at a relative humidity of 75%.

Size exclusion chromatography (SEC)

Size-exclusion chromatography (SEC) of polymers was performed on an Agilent system (series 1200) equipped with a PSS degasser, a G1310A pump, a G1362A refractive index detector and a PSS GRAM 30 and 1000 column with DMAc (+0.21 wt% LiCl) as eluent and a flow rate of 1 mL min^{-1}. The column oven was set to 40 °C and poly(ethylene oxide) (PEO) standards were used for calibration.

Conflicts of interest

The authors declare no competing financial interest.

Data availability

The data supporting this article are presented in the main article or have been included as part of the supplementary information (SI). Supplementary information is available. The Supplementary Information contains additional SLS size-distribution data, contact-angle measurements, Mössbauer spectroscopy data, and SEM control images supporting the structural characterization and redox-induced surface hydrophilization of the C4VMT/$PNAT_{30}$ coatings. See DOI: https://doi.org/10.1039/d6lp00059b.

Acknowledgements

The project has been funded by the Deutsche Forschungsgemeinschaft (DFG, German Research Foundation) – project number 391977956 – SFB1357/C02, B01 and A06. JCB further thanks the German Science Foundation (DFG) for funding within the Heisenberg-Programme (Project-ID: 517761335). Support from the keylabs (Mesoscale Characterization: Scattering Techniques, Surface and Interface Characterization, and Polymer Additives and Fillers) of the Bavarian Polymer Institute (BPI) at the University of Bayreuth is much appreciated. Marco Schwarzmann is thanked for preparing the transmission electron microscopy and scanning electron microscopy images, Beate Bojer is thanked for solid-state NMR measurements, and Daniel Hohenberger for Mößbauer spectroscopy measurements. We thank Prof. Dr A. Lerf for making the Mößbauer source available.

References

1 R. Geyer, J. R. Jambeck and K. L. Law, Production, use, and fate of all plastics ever made, *Sci. Adv.*, 2017, **3**(7), e1700782, DOI: 10.1126/sciadv.1700782.

2 J. R. Jambeck, R. Geyer, C. Wilcox, T. R. Siegler, M. Perryman, A. Andrady, R. Narayan and K. L. Law, Plastic waste inputs from land into the ocean, *Science*, 2015, **347**(6223), 768, DOI: 10.1126/science.1260352.

3 A. L. Andrady, Weathering and fragmentation of plastic debris in the ocean environment, *Mar. Pollut. Bull.*, 2022, **180**, 113761, DOI: 10.1016/j.marpolbul.2022.113761.

4 A. A. de Souza Machado, W. Kloas, C. Zarfl, S. Hempel and M. C. Rillig, Microplastics as an emerging threat to terrestrial ecosystems, *Glob. Chang. Biol.*, 2018, **24**(4), 1405, DOI: 10.1111/gcb.14020.

5 D. Eerkes-Medrano, R. C. Thompson and D. C. Aldridge, Microplastics in freshwater systems: A review of the emerging threats, identification of knowledge gaps and prioritisation of research needs, *Water Res.*, 2015, **75**, 63, DOI: 10.1016/j.watres.2015.02.012.

6 M. Scheurer and M. Bigalke, Microplastics in Swiss floodplain soils, *Environ. Sci. Technol.*, 2018, **52**(6), 3591, DOI: 10.1021/acs.est.7b06003.

7 A. F. R. M. Ramsperger, E. Bergamaschi, M. Panizzolo, I. Fenoglio, F. Barbero, R. Peters, A. Undas, S. Purker, B. Giese, C. R. Lalyer, *et al.*, Nano- and microplastics: A comprehensive review on their exposure routes, translocation, and fate in humans, *NanoImpact*, 2023, **29**, 100441, DOI: 10.1016/j.impact.2022.100441.

8 N. J. Beaumont, M. Aanesen, M. C. Austen, T. Börger, J. R. Clark, M. Cole, T. Hooper, P. K. Lindeque, C. Pascoe and K. J. Wyles, Global ecological, social and economic impacts of marine plastic, *Mar. Pollut. Bull.*, 2019, **142**, 189, DOI: 10.1016/j.marpolbul.2019.03.022.

9 S. B. Borrelle, J. Ringma, K. L. Law, C. C. Monnahan, L. Lebreton, A. McGivern, E. Murphy, J. Jambeck, G. H. Leonard, M. A. Hilleary, *et al.*, Predicted growth in plastic waste exceeds efforts to mitigate plastic pollution, *Science*, 2020, **369**(6510), 1515, DOI: 10.1126/science.aba3656.

10 W. W. Y. Lau, Y. Shiran, R. M. Bailey, E. Cook, M. R. Stuchtey, J. Koskella, C. A. Velis, L. Godfrey, J. Boucher, M. B. Murphy, *et al.*, Evaluating scenarios toward zero plastic pollution, *Science*, 2020, **369**(6510), 1455, DOI: 10.1126/science.aba9475.

11 V. Dudko, R. L. Timmins, O. Khoruzhenko, M. Röhrl, C. Greve, S. Rosenfeldt, T. Tammelin, S. Agarwal, E. M. Herzig and J. Breu, Spontaneous delamination of affordable natural vermiculite as a high barrier filler for biodegradable food packaging, *Mater. Adv.*, 2022, **3**(24), 9052, DOI: 10.1039/d2ma00734g.

12 M. Röhrl, R. L. Timmins, D. Ghosh, D. D. Schuchardt, S. Rosenfeldt, S. Nürmberger, U. Bölz, S. Agarwal and J. Breu, Green and scalable processing of water-soluble, biodegradable polymer/clay barrier films, *J. Appl. Polym. Sci.*, 2023, **140**(37), e54418, DOI: 10.1002/app.54418.

13 M. Röhrl, R. L. Timmins, S. Rosenfeldt, D. D. Schuchardt, F. Uhlig, S. Nürmberger and J. Breu, Stretchable clay nanocomposite barrier film for flexible packaging, *ACS Appl. Mater. Interfaces*, 2023, **15**(18), 22524, DOI: 10.1021/acsami.3c02504.

14 R. K. Basha, K. Konno, H. Kani and T. Kimura, Water vapor transmission rate of biomass based film materials, *Eng. Agric. Environ. Food.*, 2011, **4**(2), 37–42, DOI: 10.1016/S1881-8366(11)80018-2.
15 R. L. Timmins, A. Kumar, M. Röhrl, K. Havlíček, S. Agarwal and J. Breu, High barrier nanocomposite film with accelerated biodegradation by clay swelling induced fragmentation, *Macromol. Mater. Eng.*, 2022, **307**(6), 2100727, DOI: 10.1002/mame.202100727.
16 G. M. Guebitz and A. Cavaco-Paulo, Enzymes go big: Surface hydrolysis and functionalisation of synthetic polymers, *Trends Biotechnol.*, 2008, **26**(1), 32–38, DOI: 10.1016/j.tibtech.2007.10.003.
17 X. Zhu, M. Fryd, C. Barrero, S. Merali, C. Fecchio, A. M. Valentine and B. B. Wayland, Kinetic-mechanistic studies of P. cepacia lipase catalyzed corona charge selective micelle degradation, *J. Mol. Catal. B: Enzym.*, 2016, **133**, 187–195, DOI: 10.1016/j.molcatb.2016.08.013.
18 A. Chamas, H. Moon, J. Zheng, Y. Qiu, T. Tabassum, J. H. Jang, M. Abu-Omar, S. L. Scott and S. Suh, Degradation rates of plastics in the environment, *ACS Sustainable Chem. Eng.*, 2020, **8**(9), 3494, DOI: 10.1021/acssuschemeng.9b06635.
19 E. L. Cussler, S. E. Hughes, W. J. Ward and R. Aris, Barrier membranes, *J. Membr. Sci.*, 1988, **38**(2), 161, DOI: 10.1016/S0376-7388(00)80877-7.
20 G. D. Moggridge, N. K. Lape, C. Yang and E. L. Cussler, Barrier films using flakes and reactive additives, *Prog. Org. Coat.*, 2003, **46**(4), 231, DOI: 10.1016/S0300-9440(02)00180-7.
21 L. Chen, Y. Zhao, T. Chen, H. Bai, T. Zhang, H. Li, Q. An and S. Song, Correlation of aspect ratio of montmorillonite nanosheets with the colloidal properties in aqueous solutions, *Results Phys.*, 2019, **15**, 102526, DOI: 10.1016/j.rinp.2019.102526.
22 W. R. Falla, M. Mulski and E. L. Cussler, Estimating diffusion through flake-filled membranes, *J. Membr. Sci.*, 1996, **119**(1), 129–138, DOI: 10.1016/0376-7388(96)00106-8.
23 L. Pentráková, K. Su, M. Pentrák and J. W. Stucki, A review of microbial redox interactions with structural Fe in clay minerals, *Clay Miner.*, 2013, **48**(3), 543–560, DOI: 10.1180/claymin.2013.048.3.10.
24 J. W. Stucki, A review of the effects of iron redox cycles on smectite properties, *C. R. Geosci.*, 2011, **343**(2), 199–209, DOI: 10.1016/j.crte.2010.10.008.
25 C. Yu, W. Ji, X. Li, S. Yuan, P. Zhang and S. Pu, Critical role of mineral Fe(IV) formation in low hydroxyl radical yields during Fe(II)-bearing clay mineral oxygenation, *Environ. Sci. Technol.*, 2024, **58**(22), 9669–9678, DOI: 10.1021/acs.est.3c09986.
26 M. C. Celina, Review of polymer oxidation and its relationship with materials performance and lifetime prediction, *Polym. Degrad. Stab.*, 2013, **98**(12), 2419–2429, DOI: 10.1016/j.polymdegradstab.2013.06.024.
27 J. Sajiki and J. Yonekubo, Leaching of bisphenol A (BPA) to seawater from polycarbonate plastic and its degradation by reactive oxygen species, *Chemosphere*, 2003, **51**(1), 55–62, DOI: 10.1016/S0045-6535(02)00789-0.
28 M. Geven, R. d'Arcy, Z. Y. Turhan, F. El-Mohtadi, A. Alshamsan and N. Tirelli, Sulfur-based oxidation-responsive polymers. Chemistry, (chemically selective) responsiveness and biomedical applications, *Eur. Polym. J.*, 2021, **149**, 110387, DOI: 10.1016/j.eurpolymj.2021.110387.
29 Q. Fan, L. Wang, Y. Fu, Q. Li, Y. Liu, Z. Wang and H. Zhu, Iron redox cycling in layered clay minerals and its impact on contaminant dynamics: A review, *Sci. Total Environ.*, 2023, **855**, 159003, DOI: 10.1016/j.scitotenv.2022.159003.
30 A. D. Purceno, A. P. C. Teixeira, A. B. Souza, J. D. Ardisson, J. P. de Mesquita and R. M. Lago, Ground vermiculite as catalyst for the Fenton reaction, *Appl. Clay Sci.*, 2012, **69**, 87, DOI: 10.1016/j.clay.2012.08.010.
31 C. M. Geiselhart, W. Xue, C. Barner-Kowollik and H. Mutlu, Degradable redox-responsive polyolefins, *Macromolecules*, 2021, **54**(4), 1775, DOI: 10.1021/acs.macromol.1c00010.
32 R. Kilic Boz, D. Aydin, S. Kocak, B. Golba, R. Sanyal and A. Sanyal, Redox-responsive hydrogels for tunable and "on-demand" release of biomacromolecules, *Bioconjugate Chem.*, 2022, **33**(5), 839, DOI: 10.1021/acs.bioconjchem.2c00094.
33 C. Lin, H. Hu, H. Zhu, Q. Luan, Z. Li, J. Wang and J. Zhu, Disulfide-driven on-demand degradation of the PBAT copolymer: Stable comprehensive performance, long-term storage, and redox-induced degradation, *Macromolecules*, 2025, **58**(8), 4170, DOI: 10.1021/acs.macromol.4c02244.
34 N. Ziegenbalg, J. Eberhardt, S. Städter, S. Höppener, S. Stumpf and J. C. Brendel, Monodisperse oxidative-sensitive polymer nanoparticles from dispersion polymerization of N-acryloyl thiomorpholine, *Eur. Polym. J.*, 2023, **196**, 112258, DOI: 10.1016/j.eurpolymj.2023.112258.
35 J. O'Loughlin, D. Doherty, B. Herward, C. McGleenan, M. Mahmud, P. Bhagabati, A. N. Boland, B. Freeland, K. D. Rochfort, S. M. Kelleher, *et al.*, The potential of bio-based polylactic acid (PLA) as an alternative in reusable food containers, a review, *Sustainability*, 2023, **15**(21), 15312, DOI: 10.3390/su152115312.
36 T. A. Swetha, A. Bora, K. Mohanrasu, P. Balaji, R. Raja, K. Ponnuchamy, G. Muthusamy and A. Arun, A comprehensive review on polylactic acid (PLA) – Synthesis, processing and application in food packaging, *Int. J. Biol. Macromol.*, 2023, **234**, 123715, DOI: 10.1016/j.ijbiomac.2023.123715.
37 R. A. Auras, B. Harte, S. Selke and R. Hernandez, Mechanical, physical, and barrier properties of poly (lactide) films, *J. Plast. Film Sheeting*, 2003, **19**(2), 123–135, DOI: 10.1021/acs.est.1c01512.
38 M.-B. Coltelli, F. Cartoni, L. Panariello, L. Aliotta, V. Gigante and A. Lazzeri, Assessing PLA/PBSA films for sustainable packaging for moist and perishable foods, *Polymers*, 2025, **17**(23), 3093, DOI: 10.3390/polym17233093.
39 S. Yue, T. Zhang, S. Wang, D. Han, S. Huang, M. Xiao and Y. Meng, Recent progress of biodegradable polymer package materials: Nanotechnology improving both oxygen and water vapor barrier performance, *Nanomaterials*, 2024, **14**(4), 338, DOI: 10.3390/nano14040338.
40 S. Yao, X. Li, T. Wang, X. Jiang, Y. Song and H. P. H. Arp, Soil metabolome impacts the formation of the eco-corona and

adsorption processes on microplastic surfaces, *Environ. Sci. Technol.*, 2023, **57**(21), 8139, DOI: 10.1021/acs.est.3c01877.

41 C. A. Gorski, M. Aeschbacher, D. Soltermann, A. Voegelin, B. Baeyens, M. Marques Fernandes, T. B. Hofstetter and M. Sander, Redox properties of structural Fe in clay minerals. 1. Electrochemical quantification of electron-donating and -accepting capacities of smectites, *Environ. Sci. Technol.*, 2012, **46**(17), 9360–9368, DOI: 10.1021/es3020138.

42 C. A. Gorski, L. Klüpfel, A. Voegelin, M. Sander and T. B. Hofstetter, Redox properties of structural Fe in clay minerals. 2. Electrochemical and spectroscopic characterization of electron transfer irreversibility in ferruginous smectite, SWa-1, *Environ. Sci. Technol.*, 2012, **46**(17), 9369–9377, DOI: 10.1021/es302014u.

43 C. A. Gorski, L. E. Klüpfel, A. Voegelin, M. Sander and T. B. Hofstetter, Redox properties of structural Fe in clay minerals: 3. Relationships between smectite redox and structural properties, *Environ. Sci. Technol.*, 2013, **47**(23), 13477–13485, DOI: 10.1021/es403824x.

44 A. Neumann, S. Petit and T. B. Hofstetter, Evaluation of redox-active iron sites in smectites using middle and near infrared spectroscopy, *Geochim. Cosmochim. Acta*, 2011, **75**(9), 2336–2355, DOI: 10.1016/j.gca.2011.02.009.

45 V. Pothanamkandathil, A. Neumann, A. Thompson and C. A. Gorski, Redox properties of structural Fe in clay minerals: 4. Reinterpreting redox curves by accounting for electron transfer and structural rearrangement kinetics, *Environ. Sci. Technol.*, 2024, **58**(44), 19702–19713, DOI: 10.1021/acs.est.4c07835.

46 L. Infante Teixeira, K. Landfester and H. Thérien-Aubin, Selective oxidation of polysulfide latexes to produce polysulfoxide and polysulfone in a waterborne environment, *Macromolecules*, 2021, **54**(8), 3659, DOI: 10.1021/acs.macromol.1c00382.

47 G. Socrates, *Infrared and Raman Characteristic Group Frequencies: Tables and Charts*, John Wiley & Sons, 2004.

48 B. Sjöberg, S. Foley, B. Cardey, M. Fromm and M. Enescu, Methionine oxidation by hydrogen peroxide in peptides and proteins: A theoretical and Raman spectroscopy study, *J. Photochem. Photobiol., B*, 2018, **188**, 95, DOI: 10.1016/j.jphotobiol.2018.09.009.

49 A. Torreggiani, S. Barata-Vallejo and C. Chatgilialoglu, Combined Raman and IR spectroscopic study on the radical-based modifications of methionine, *Anal. Bioanal. Chem.*, 2011, **401**(4), 1231, DOI: 10.1007/s00216-011-5203-0.

50 F. H. Sobotta, M. T. Kuchenbrod, F. V. Gruschwitz, G. Festag, P. Bellstedt, S. Hoeppener and J. C. Brendel, Tuneable time delay in the burst release from oxidation-sensitive polymersomes made by PISA, *Angew. Chem., Int. Ed.*, 2021, **60**(46), 24716–24723, DOI: 10.1002/anie.202108928.

51 S. M. Tiquia-Arashiro and D. Pant, *Microbial Electrochemical Technologies*, CRC Press, Taylor & Francis Group, 2020.

52 M. D. Dyar, D. G. Agresti, M. W. Schaefer, C. A. Grant and E. C. Sklute, Mössbauer spectroscopy of earth and planetary materials, *Annu. Rev. Earth Planet. Sci.*, 2006, **34**(1), 83–125, DOI: 10.1146/annurev.earth.34.031405.125049.

53 A. Manceau, V. A. Drits, B. Lanson, D. Chateigner, J. Wu, D. Huo, W. P. Gates and J. W. Stucki, Oxidation-reduction mechanism of iron in dioctahedral smectites: II. Crystal chemistry of reduced Garfield nontronite, *Am. Mineral.*, 2000, **85**(1), 153–172, DOI: 10.2138/am-2000-0115.

54 E. Murad, Mossbauer spectroscopy of clays, soils and their mineral constituents, *Clay Miner.*, 2010, **45**(4), 413–430, DOI: 10.1180/claymin.2010.045.4.413.

55 K. Efimenko, J. A. Crowe, E. Manias, D. W. Schwark, D. A. Fischer and J. Genzer, Rapid formation of soft hydrophilic silicone elastomer surfaces, *Polymer*, 2005, **46**(22), 9329, DOI: 10.1016/j.polymer.2005.07.046.

56 F. Rios and S. Smirnov, Biochemically responsive smart surface, *ACS Appl. Mater. Interfaces*, 2009, **1**(4), 768, DOI: 10.1021/am800166t.

57 F. Uhlig, A. M. Stich, S. Rosenfeldt and J. Breu, Delamination of vermiculite into ultrahigh-aspect-ratio nanosheets, *Z. Anorg. Allg. Chem.*, 2026, DOI: 10.1002/zaac.70139.

58 D. R. Lovley, S. J. Giovannoni, D. C. White, J. E. Champine, E. J. P. Phillips, Y. A. Gorby and S. Goodwin, *Geobacter metallireducens* gen. nov. sp. nov., a microorganism capable of coupling the complete oxidation of organic compounds to the reduction of iron and other metals, *Arch. Microbiol.*, 1993, **159**(4), 336–344, DOI: 10.1007/BF00290916.

59 F. H. Sobotta, M. T. Kuchenbrod, C. Grune, D. Fischer, S. Hoeppener and J. C. Brendel, Elucidating preparation-structure relationships for the morphology evolution during the RAFT dispersion polymerization of N-acryloyl thiomorpholine, *Polym. Chem.*, 2021, **12**(11), 1668–1680, DOI: 10.1039/D0PY01697G.

60 C. Prescher, C. McCammon and L. Dubrovinsky, MossA: A program for analyzing energy-domain Mossbauer spectra from conventional and synchrotron sources, *J. Appl. Crystallogr.*, 2012, **45**(2), 329–331, DOI: 10.1107/S0021889812004979.